Journal of Applied Physics

RESEARCH ARTICLE | NOVEMBER 20 2025

Experiments on thiophene pyrolysis using gas-phase Raman spectroscopy

M. Kuvshinov ✉ ; L. Weller ; S. Hochgreb

J. Appl. Phys. 138, 193105 (2025)
https://doi.org/10.1063/5.0288669

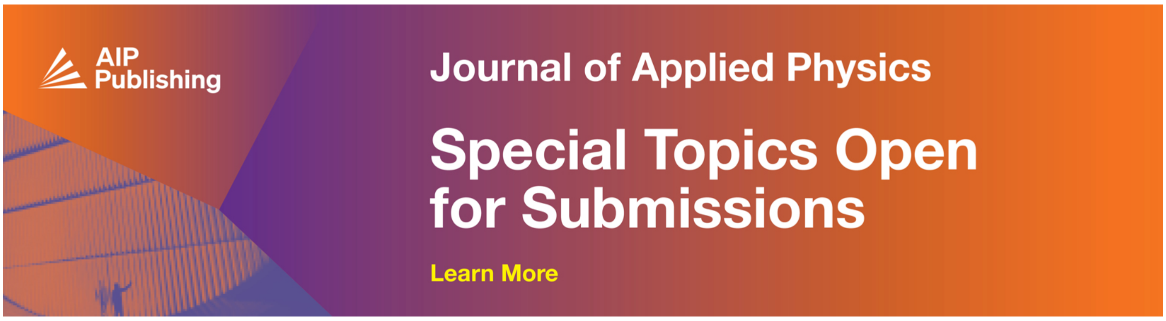

AIP Publishing

Journal of
Applied Physics

ARTICLE

pubs.aip.org/aip/jap

Experiments on thiophene pyrolysis using gas-phase Raman spectroscopy

Cite as: J. Appl. Phys. **138**, 193105 (2025); doi: 10.1063/5.0288669
Submitted: 2 July 2025 · Accepted: 30 October 2025 ·

M. Kuvshinov,[a)] L. Weller, and S. Hochgreb

AFFILIATIONS

Department of Engineering, University of Cambridge, Cambridge, United Kingdom

[a)]**Author to whom correspondence should be addressed:** mk887@cantab.ac.uk

ABSTRACT

Recent studies have demonstrated the capability of floating catalyst chemical vapor deposition (FC-CVD) synthesis to continuously produce direct-spun carbon nanotube (CNT) fibers with useful properties. Insufficient knowledge of chemical processes underpinning CNT growth via FC-CVD, due to lack of *in situ* measurements, remains a major limitation in understanding how to intensify the production of high-quality material. Thiophene is a key precursor to the formation of CNTs in H_2 gas environments. A pulsed, gas phase laser Raman spectroscopy system was implemented to perform measurements of thiophene concentrations and mixture temperatures during the CNT synthesis process via FC-CVD in a cross flow reactor. From these measurements, it was possible to evaluate thiophene thermal decomposition at reactor temperatures between 20 and 1100 °C, as well as Raman signatures of the main products of thiophene decomposition. These measurements represent the first *in situ* Raman measurements performed in a FC-CVD CNT synthesis reactor.

I. INTRODUCTION

Carbon nanotube (CNT) is a material with a unique blend of remarkable characteristics.[1] With appropriate modifications to their structure, CNT materials can outperform conventionally used materials for the purposes of thermal and electrical conductivity, mechanical flexibility or rigidity, adsorption, and catalytic purposes.[2–5] As such, CNTs have already been used in various applications such as electronic and electromagnetic shielding, solid-heat conductors, additives to material composites, and replacements for carbon fiber. However, difficulties in mass-scale manufacture with uniform, tailored material parameters have been a major hurdle in wide-scale application of CNTs.

The synthesis of high-quality, high-purity CNT materials has been limited to batch-based processes,[6,7] which are not able to meet the growing demand for mass CNT production.[1] At present, floating catalyst chemical vapor deposition (FC-CVD) is regarded as the most developed and simplest way to grow CNTs continuously in a laboratory and semi-pilot scales.[8–10] One of the promising variations of the process involves growing CNTs in a hot-wall reactor over a sufficiently long residence time and high enough concentration that the molecules self-assemble into a continuous CNT network known as an aerogel. The aerogel can be continually extracted from the back-end of the reactor and wound onto a motorized bobbin to produce fibers or mats.[11] This results in bulk CNT materials that can be produced in a single-step process.

A number of invasive sampling techniques have been utilized to study compounds within the process. Hoecker *et al.* have used a sampling probe to perform *in situ* axial measurement of catalyst particle size distributions along the centerline of the reactor as a function of furnace set-temperature using a scanning mobility particle sizer.[11] The same authors have used a commercially available Fourier-Transform Infrared (FTIR) analyzer on extracted exhaust gas samples to study the decomposition of thiophene and ferrocene as a function of furnace set-temperature. In later work, the same authors have performed axial measurements of aerogel formation as a function of hydrocarbon source by determining the accumulated mass on the circular alumina filters.[12] While these techniques are able to provide some information on the underlying processes of the aerogel synthesis, they fail to detect intermediate species and, due to their invasive nature, may have an effect on the observed measurements. Furthermore, the inability to instantaneously quench samples at their formation temperature may result in misleading conclusions. Nevertheless, understanding of the process control variables does exist on a semi-empirical basis,[13–15] by varying various input parameters such as reactant stoichiometry, furnace temperature, residence time, and reactor dimensions, while observing how these affect the final aerogel product characteristics.

To date, there have been no publications demonstrating any *operando*, non-invasive optical measurements during CNT synthesis via FC-CVD. As a consequence, details of the synthesis process, such as underlying chemical reactions, nucleation, and agglomeration mechanisms of CNT aerogel formation, are still not quantified or understood. The difficulties surrounding optical access are the main barriers for directly probing the environment inside hot furnaces. Major modifications to the reactor tube are required, leading to difficult engineering challenges.

The present work describes the first application of an optical diagnostic technique leading to non-intrusive *in situ* diagnostics of gas phase species surrounding thiophene breakdown in CNT formation in an FC-CVD reactor. The pyrolytic decomposition of thiophene is studied in particular, as the process serves as a promoter of CNT growth, as well as a promoter of catalyst nanoparticle nucleation.[8,16] Its thermal decomposition has been experimentally studied in various environments, such as shock tubes, silica reactors, and vertical furnaces. The products of decomposition have been observed to be consisting of benzene, hydrogen, ethene, acetylene, methane, and hydrogen sulfide, along with lower levels of dithiophenes, depending on the temperature (800°–1050°), the atmosphere and carrier gases used.[17–21] This study focuses on the analysis of product formation of thiophene decomposition in FC-CVD specific conditions.

Spontaneous Raman spectroscopy was chosen as the investigative technique, as it is able to simultaneously detect multiple species and provide quantitative measurements, in the present case, species molar fractions and gas temperatures. In what follows we describe the modifications to the reactor, the resulting species measurements, and some of the challenges that must still be overcome for fully quantitative assessments.

II. EXPERIMENTAL SETUP

A. Spontaneous Raman spectroscopy setup

The configuration schematic of the Raman signal delivery and collection system is shown in Fig. 1. The excitation beam was provided by a high-frequency Litron LDY300 pulsed laser **(PL)**, Nd:YLF type with a dual cavity system and emission centered at 527 nm, with a pulse length of 300 ns, which provided an elliptical beam shape of 10 × 2 mm^2 along the major and minor axes, respectively.

The energy per pulse at the chosen operating condition of 1.5 kHz and 70% maximum current was measured as 38 mJ when operated in dual pulse mode with pulses temporally overlapped. The laser beam was guided by two highly reflective, high energy 532 nm mirrors, **M1** and **M2**, onto a long-pass dichroic filter (LPD02-532RU-25), **DF**, centered at 532 nm (10 nm FWHM). The dichroic filter acted as a mirror in the direction of the laser beam propagation, which reflected the beam at 90° onto another high reflectivity, high energy resistant broadband mirror, **BM**, that sent the beam through a 50 mm diameter lens, **L1**, with a focal length of $f = 400$ mm toward the center of the reactor.

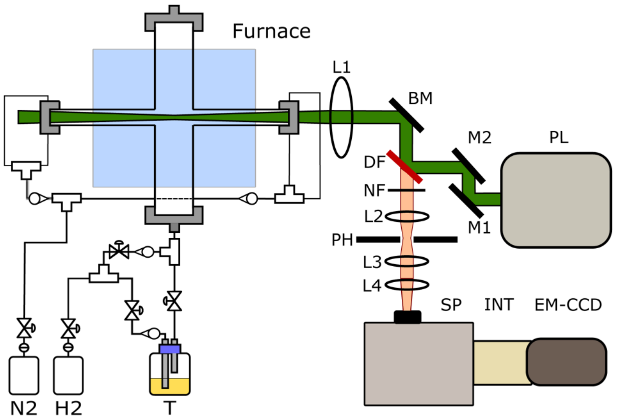

FIG. 1. Schematic of pulsed laser backscatter collection, free-coupled, confocal Raman spectroscopy setup. PL, pulsed laser diode; M, mirror; L, lens; BM, broadband mirror; DF, dichroic filter; NF, notch filter; PH, pinhole; SP, spectrograph; INT, intensifier; EM-CCD, electron-multiplying charge-coupled device.

The spontaneous Raman emission was collected in a backscattering, free-coupled, confocal configuration. The Raman emission was generated along the path of the laser beam and was collected by optical elements along the beam delivery path, via the lens **L1**, broadband mirror **BM** and a long-pass dichroic filter **DF**. The setup allows for prompt alignment of Raman emission generation and collection as only one point of optical access is required. From the impinged emission, the long-pass dichroic filter transmitted the Raman-generated Stokes photons. The Rayleigh scattered green laser light was reflected back toward the laser, along with the Anti-Stokes photons. The collimated Stokes emission was separated from the residual Rayleigh scattered emission via a notch filter, **NF** (centered at 532 nm with an FWHM of 10 nm) and focused by a 25 mm diameter lens, **L2**, with a focal length of 50 mm, onto a $50\,\mu$m pinhole, **PH**, to prevent stray light from entering the collection path. Beyond the pinhole, the Raman emission was recollimated using a 25 mm diameter, $f = 50$ mm lens, **L3**, and focused by a 25 mm diameter lens, **L4**, with $f = 50$ mm onto the slit set to $1000\,\mu$m located in the side input port of the Shamrock-303i spectrograph, **SP**.

An Invisible Vision UVi Camera Intensifier (Model 2550-10), **INT**, was used as an electronic shutter in order to reject light from competing spectroscopic processes. The shutter time was set to 300 ns (corresponding to the laser pulse width), at a 65% gain setting. The shutter was triggered by the positive edge of the laser sync output. The intensifier was attached to the spectrograph output port via a 3D-printed coupling mount, which blocked stray light. Particular care was taken to ensure that the focal planes of the spectrograph and the intensifier coincided, by placing the intensifier and the coupled EM-CCD on a single-axis mounting rail for fine adjustments. An EM-CCD, Andor Ixon Ultra-888 (1024 × 1024 pixels) was coupled to the output of the intensifier by a Nikon F-mount lens. The camera was thermoelectrically cooled to −40 °C. The camera was externally triggered by the rising edge of the laser sync output, with the exposure window set to its lowest setting of 10 μs.

The spectrograph prism grating was set to 1200 lines/mm in order to achieve sufficiently high resolution of the target species Raman modes. For this resolution, the wavelength space of interest had to be separated into nine acquisition sections, covering a range from 255 to 4260 cm^{-1}. Acquisition in each section consisted of 6000 shots with the vertical camera binning over 46 pixels, resulting in a collection system acquisition frequency of 136 Hz. The acquisition regions were defined in such a way that each adjacent section had at least a 30% wavenumber overlap with the neighboring sections to facilitate stitching into one single spectrum.

B. Reactor tube design

Two different reactor geometries, cylindrical and cross-flow, were tested. The reactors were manufactured out of fused quartz by Cambridge Glass-blowing company. Quartz was chosen for its high-temperature resistance, chemical inertness, and optical transparency in the 275–2000 nm range.

The plain cylindrical reactor was tested first, as this is the normal configuration used in investigative and commercial FC-CVD applications. The tube had an inner radius of 23.2 mm with a wall thickness of 2.2 mm and a length of 700 mm. The ends of the reactor were sealed off with the use of stainless steel sandwich flanges and Viton O-rings. A single 6 mm gas fitting was welded into each flange for inlet and outlet of gases.

The reactor was placed inside an electrically heated, horizontally split furnace (Elite Thermal Systems Ltd., TSHH12/90/305/3216CC), provided with a single heating zone with a maximum operating temperature of 1200 °C. The heating volume had a length of 300 mm and a width of 150 mm.

Fiberglass insulation was used to pad out the contact areas of two halves of the furnace, forming a layer with a thickness of 5–10 mm to improve the furnace heat retention. The furnace tube rests were also padded with insulation to raise the tube height such that the laser beam, aligned parallel to the horizontal, entered the tube in a direction normal to its wall.

Preliminary Raman measurements were performed using a mixture of 3% molar concentration of thiophene in a hydrogen environment, heated between 20 and 1000 °C. Such molar concentrations were chosen to be in line with conditions encountered in aerogel-spinning studies.[11] At 800 °C, solid state deposition was observed to form on the locations where the cylindrical tube intersected laser light, presumably due to photolysis catalyzed by the laser beam. The wall deposition resulted in strong broadband emission spectra, which overwhelmed the Raman signal emission.

In order to maintain continuous optical access to the reacting zone, the cylindrical reactor geometry was altered into a cross configuration with the addition of orthogonal channel tubes positioned at the middle point of the reactor, which carry continuous purge gas flow toward its center, preventing recirculation of decomposition products into the cross channels or formation of solid deposition on walls. These counterflowing purging channels of inner diameter 15.7 and 2.5 mm wall thickness extended by 300 and 350 mm from the reactor tube's wall, respectively, resulting in a total length of 323.2 and 373.2 mm from the center of the reactor tube. The furnace hinge was raised with the use of steel blocks to allow the purging channels to protrude out of the clamshell furnace. The purging channel geometry allowed a focused laser beam to reach the sampling volume at the center of the reactor and pass through the furnace without impinging on any surfaces.

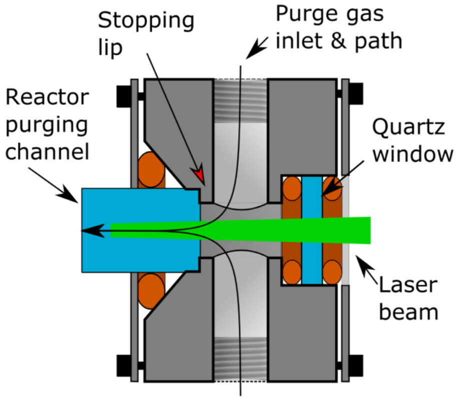

FIG. 2. Schematic of the purging flange.

The ends of the purging channels were closed off with purging flanges, a schematic of which is shown in Fig. 2. Each one of the flanges consists of three parts—two retaining plates and the main body. Two 1/8 in. NPT holes were placed in the center of the main body through which the purging gas enters the flange. One section of the body contains a 25 mm diameter, 3 mm thick quartz window with anti-reflective coating, which is sandwiched between two Viton O-rings, held in place by the retaining plate. This provides an airtight seal and a flat optical window for laser injection. The second section of the flange couples the purging system to the reactor tube.

An undesirable side effect of the back-scattering confocal configuration of the Raman signal collection is that the collection of Raman emission from the species present takes place along the entirety of the collection path, such as the purging channels and the outside environment of the reactor. In order to mitigate the problem, N_2 was used as a purging gas to differentiate between the Raman emission generated from the species of interest carried by H_2 in the central reactor flow.

However, the difference in densities of N_2 and H_2 has resulted in complex, non-plug-flow gas dynamics within the reactor. The gases from the central flow are transported into the upper regions of the purging channels by differential density gravitational effects. The purging gases create an inert boundary layer close to the injection points at the flanges, which moves to the bottom of the central flow channel. The containment of the central hydrogen flow within the reactor improves as a function of temperature, reducing the overall volume fraction of purge gas in the Raman probe volume. A detailed explanation of the gas dynamics, with the use of numerical modeling, and its impact on the measurement volume can be found in the supplementary material.

C. Experimental conditions

The species of interest for this study were as follows: hydrogen as carrier gas, thiophene as promoter, and nitrogen as a purging gas. Hydrogen and nitrogen gases were delivered by Alicat MC-5SLPM-D mass flow controllers with a ±0.6% precision at ambient conditions and injected directly into the reactor.

A liquid bubbler, maintained at 0 °C by an ice/water mixture, was used to evaporate thiophene at a controlled rate by the H_2 carrier gas. The molar fractions were calculated using the Antoine equation,[22]

$$\log P_v = A - \frac{B}{C+T}, \tag{1}$$

where A = 4.073 58, B = 1239.578 and C = −52.585 and T = 293.15.

The two variables of interest in the thiophene decomposition study were the inlet thiophene molar fraction and the furnace set-point temperature. The investigated experimental conditions are listed in Table I. At each temperature, six conditions with different input thiophene molar fractions were established by varying the hydrogen flow through the thiophene bubbler and the hydrogen dilution flow, respectively, for a constant total volumetric flow of 0.5 SLPM inside the reactor. The two flows were mixed at a T-junction located 200 mm upstream of the injection location into the reactor. The molar and mass rates per each condition are also shown in Table I. The maximum thiophene molar concentration in the proposed experiments did not exceed 3%. Such limit was set to keep in line with the experimental conditions used in earlier studies of the CNT synthesis via FC-CVD.[23,24] Nitrogen gas was used for purging at a flow rate of 0.05 SLPM in each purging channel. For all results presented in the following section, background signals were obtained while flowing 100% N_2 in the reactor and purging channels.

III. IN SITU MEASUREMENTS OF GAS TEMPERATURE BY FULCHER-α HYDROGEN BANDS

Potential temperature non-uniformities can occur within the reactor owing to incomplete enclosure of the reactor within the heating volume and mixing of purge gases, which can result in uncertainties when measuring the concentration of trace species. Thermocouples provide precise temperature measurements and are commonly used in an *in situ*. However, they cannot be used simultaneously with the constructed Raman setup at the measurement location, due to the presence of the high energy laser beam.

TABLE I. Experimental conditions for thiophene thermal decomposition study. Listed: hydrogen standard volumetric flow $\dot{Q}$ for dilution and bubbler and expected inlet molar fraction of thiophene inside the reactor based on the Antoine equation.[22] Each experiment was repeated at furnace set-point temperatures of 20, 300, 500, 700, 800, 900, 1000, and 1100 °C.

Expt. #	$\dot{Q}_{dilution}/\dot{Q}_{bubbler}$ (SLPM)	Molar fraction (H_2/thiophene)
1	0.5/0.0	1.000/0.000
2	0.4/0.1	0.994/0.006
3	0.3/0.2	0.988/0.012
4	0.2/0.3	0.982/0.018
5	0.1/0.4	0.976/0.024
6	0.0/0.5	0.970/0.030

In order to determine the local temperature at which the Raman spectra were recorded, temperatures were extracted from the acquired H_2 Raman spectra and compared with the furnace set point temperatures performed prior.

Temperatures were determined from the relative population density distributions between excited molecular states of H_2, a method employed for *in situ* temperature measurements of molecular plasmas and gases,[25–27] where the method has been shown to be in good agreement with other temperature measurement methods such as Doppler broadening,[28] Coherent anti-Stokes Raman scattering (CARS),[29] and thermocouple results. A brief explanation of the method is given below, based on a detailed derivation provided in Ref. 30.

The emission intensity $I_{\mathbf{n}}^{\mathbf{n}'}$ is the power emission per unit volume emitted during a transition between states $\mathbf{n}' \rightarrow \mathbf{n}$, where $\mathbf{n} = (n, v, j)$ is a set of electronic, vibrational, and rotational quantum state numbers is indicated as[26]

$$I_{\mathbf{n}}^{\mathbf{n}'} = \frac{hc}{\lambda} N_{\mathbf{n}'} A_{\mathbf{n}}^{\mathbf{n}'}, \tag{2}$$

where h, c, and λ represent Planck's constant, the speed of light, and wavelength of the emission, respectively, $N_{\mathbf{n}'}$ represents the number population density of the rovibronic level of interest, and $A_{\mathbf{n}}^{\mathbf{n}'}$ corresponds to the rate of spontaneous emission.

The Fulcher-α spectrum of H_2 arises from the transition from the $d^3\Pi_u$ into the $a^3\Sigma_g^+$ state. The upper electronic state is split into the $d^3\Pi_u^+$ and $d^3\Pi_u^-$ states because of λ-doubling. Due to optical selection rules, the Q-branch of the Fulcher-α transition originates only from the $d^3\Pi_u^-$ state. For $d^3\Pi_u^-, v', j' \rightarrow, a^3\Sigma_g^+, v, j$ transitions, the rovibronic transition probabilities are assumed to be independent of the rotational quantum number j according to the Hönl–London principle. In addition, the effective lifetime of the excited state is much shorter than the relaxation time such that the radiative lifetime for each rovibronic level within the $d^3\Pi_u^-$ is the same, for example, $v' = 2 (j = 1, 2, 3, 4, \ldots)$ is equivalent to $39.5 \pm 1.9 \times 10^{-9}$ s.[30] The diagonal vibrational transitions with $v' = v$ are the most intense emission bands within the electronic transition. Therefore, in the present calculations, we have considered the $d^3\Pi_u^-(v = 2) \rightarrow, a^3\Sigma_g^+, (v' = 2)$, rotational transitions.[31]

The rotational and translational energy exchanges are considered in thermal equilibrium. As the upper levels are only populated via the lower level rotational distribution, the temperature obtained from these levels can be considered a valid estimation of the temperature. As such, the temperature relation for the population of the $d^3\Pi_u^-$ $(v = 2)$ rotational level can be expressed as[31]

$$\frac{N_{\mathbf{n}'}}{g_j} \propto \frac{I_{n'}^{n}}{\left(v_{n'}^{n}\right)^3 g_j} \propto \exp\left(-\frac{E_{X0j}}{T_{rot}}\right), \tag{3}$$

where $N_{n'}$ is the level population, $I_{n'}^{n}$ is the intensity of a spectral line, $v_{n'}^{n}$ is the wavenumber of the radiative transition, E_{X0j} is

TABLE II. Transition parameters for the first seven lines of (2-2) Q branch of Fulcher-α band of hydrogen molecule.[31]

Line	E_{X0j} (K)	$\nu_{n'}^{n}$ (cm^{-1})	j	$g_{a,s}$	g_j
Q(1)	170.5	4155.234	1	3	9
Q(2)	509.8	4143.447	2	1	5
Q(3)	1015.1	4125.855	3	3	21
Q(4)	1681.6	4102.565	4	1	9
Q(5)	2503.8	4074.000	5	3	33
Q(6)	3304.0	4039.478	6	1	13
Q(7)	4279.7	4000.044	7	3	45

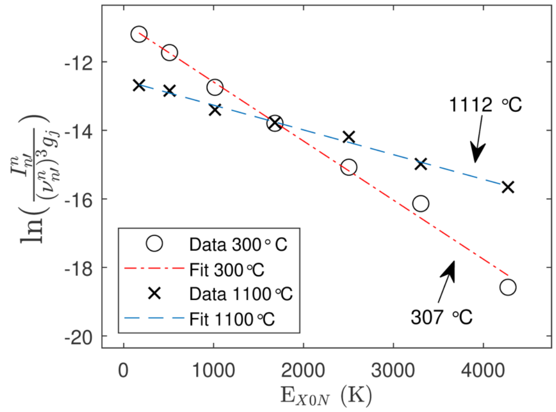

FIG. 4. Best fits of temperature based on intensity values and E_{XON} degeneracy and level numbers in Table II.

rotational energy of the ground state (K), T_{rot} is rotational temperature (K), and $g_j = g_{a,s}(2j+1)$ is the total degeneracy of the lower rotational level with the nuclear spin, $g_{a,s}$ equal to 3 for even, or 1 for odd rotational levels.

The transition parameters for the lines of (2-2) Q branch of the Fulcher-α band are listed in Table II.[32–34]

Figure 3 shows measured intensities of Raman signal emissions of pure hydrogen rovibronic transitions $Q(j)$ (where j = 1–7) as a function of furnace set-point temperature (Experiment number 1 in Table I). The mode intensities were normalized to the magnitude of the Q(1) H_2 mode.

Temperature can then be determined by expressing Eq. (3) in a logarithmic form,

$$\ln\left(\frac{I_{n'}^{n}}{(\nu_{n'}^{n})^3 g_j}\right) = -\frac{E_{X0j}}{T_{rot}} + C, \tag{4}$$

where C is a constant that combines all of the factors that are independent of the rotational quantum number. Equation (4) allows the gas temperature in the hydrogen stream to be calculated as a best fit slope from the measured peak intensity values, using the E_{X0j} rovibronic term values of the ground states provided in Table II. Examples of such best fits are shown in Fig. 4, for the logarithm of experimentally acquired reduced Raman mode intensities at inlet X_{H_2} = 1.0 and furnace set-point temperatures of 300 (red) and 1100 (blue) °C. The extracted gas temperature values from the Raman spectra are in good agreement with the furnace set-point temperatures.

Figure 5 shows the temperatures measured within the center of the reactor using the presently described technique for (Expt. 1 in Table I), as well as measurements made with a sheathed type-K thermocouple. The thermocouple measurements were not corrected for radiation.

The extracted temperatures from the Raman signal are in good agreement with the thermocouple measurements up to

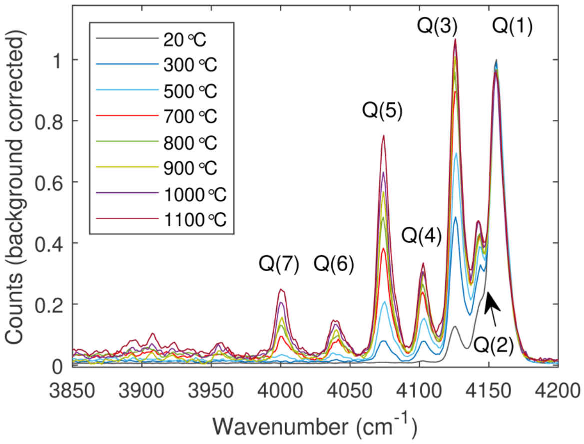

FIG. 3. Raman signal measured from excitation to the ground level from the indicated Q modes of pure hydrogen gas, as a function of furnace set-temperature.

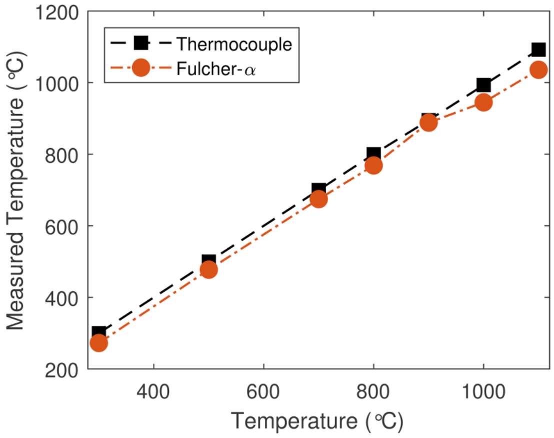

FIG. 5. Gas temperature values measured at the center of the reactor via the Fulcher-α band technique and sheathed thermocouple, as a function of furnace set point temperature for Expt. 1 in Table I.

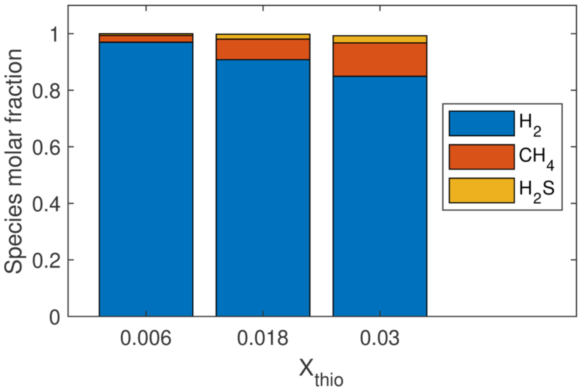

FIG. 6. Resultant equilibrium calculations molar fractions of major species of thiophene decomposition at 1100 °C mixture temperature and atmospheric pressure for experimental conditions 2, 4, and 6 listed in Table I.

800 °C, with the discrepancy between two data sets increasing at higher temperatures. This can be attributed to the decreasing signal to noise ratio (SNR) and the increasing number of the observable transition lines with increasing temperatures, owing to the lower molar densities and molecular population distribution across many more modes.

Overall, the small temperature difference between furnace set point and measured temperature with the N_2-purging conditions shows that the carrier gas containing species of interest was efficiently contained in the central sampling region of the gas and in the region of uniform temperature.

IV. THIOPHENE DECOMPOSITION STUDY

A. Thiophene pyrolytic thermal decomposition

Preliminary thermodynamic equilibrium calculations were performed in order to predict the expected products of thiophene decomposition for the presented system. Calculations were performed using the equilibrium model in Cantera,[35] which included thermodynamic data for 125 species distributed in gas, liquid, and solid phases,[36] as a function of fraction of thiophene in hydrogen. However, there were no species included with longer than two carbon bonds.

The calculations were performed for experimental conditions 2, 4, and 6 listed in Table I at atmospheric pressure and 1100 °C. The resultant molar fractions of major species in the gas phase are shown in Fig. 6.

Only the bath gas hydrogen (H_2), methane (CH_4), and hydrogen sulfide (H_2S) are expected as major species present in the gas phase at equilibrium. An increase of thiophene molar fraction in the initial gas mixture leads to an increase in CH_4 as a final product. Minor equilibrium product species, with molar fractions less than 0.01, are ethene, acetylene, and carbon disulfide.

B. Raman emission results for thiophene pyrolysis

Figure 7 shows the Raman spectra for X_{thio} = 0.03 thiophene inlet molar fraction at 20 and 1100 °C, respectively (Expt. 6 in Table I). The mode intensities were normalized to the magnitude of the Q(1) H_2 mode. At 20 °C, we observe the pure hydrogen

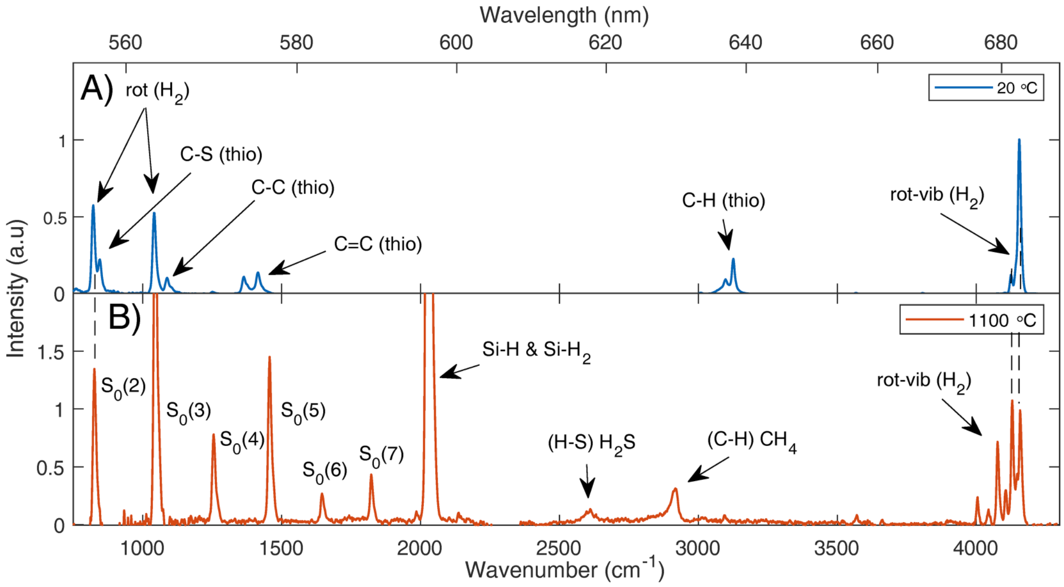

FIG. 7. Raman spectra for initial molar fraction of thiophene of $X_{thio} = 0.03$ at (a) 20 °C and at (b) 1100 °C furnace set-point temperature, over a range of wavenumbers containing relevant modes.

TABLE III. List of observed thiophene modes. Modes marked by (*) overlap with a position of H_2 Raman modes.

Mode #	Expt. freq (cm^{-1})	Assignment
1	846	C—S (v)
2	1088	C—H (δ) C═C (v)
3	1365	C═C (v)
4	1415	C═C (v)
5*	3098	C—H (v)
6	3126	C—H (v)

ro-vibrational modes, as well as the bands of C—S, C—C, C═C, and C—H bonds of the unreacted thiophene. At 1100 °C, hydrogen modes shift slightly, which higher energy ro-vibrational modes appearing, while the original thiophene bonds disappear. Instead, bonds associated with H_2S and CH_4 appear, along with evidence of Si—H bonds, possibly etched from the quartz tube, as discussed further on.[37,38] Table III lists the locations and bond assignments of the six observed independent thiophene modes.

C. Signatures of Raman emission as a function of temperature and concentration

Figures 8 and 9 show the evolution of Raman spectra of the thiophene-H_2 mixture as a function of temperature, for $X_{thio} = 0.03$ (Expt. 6 from Table I) over a range of wavenumbers. Figure 8 highlights the details of a region of the Raman spectra over a narrow region at low wavenumbers, containing both C═C modes of thiophene and the $S_0(5)$ mode for hydrogen. The intensity of the observed thiophene modes at 1365 and 1415 cm^{-1} decreases up to 800 °C due to an increase in temperature and a consequent decrease in molecular density, beyond which the modes become indistinguishable from the noise floor, as the concentration decreases owing to reaction.

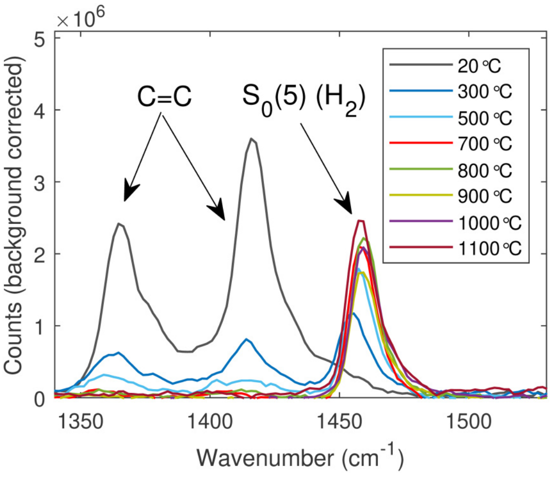

FIG. 8. Raman spectra as a function of temperature for inlet molar fraction $X_{thio} = 0.03$ for the low wavenumber range.

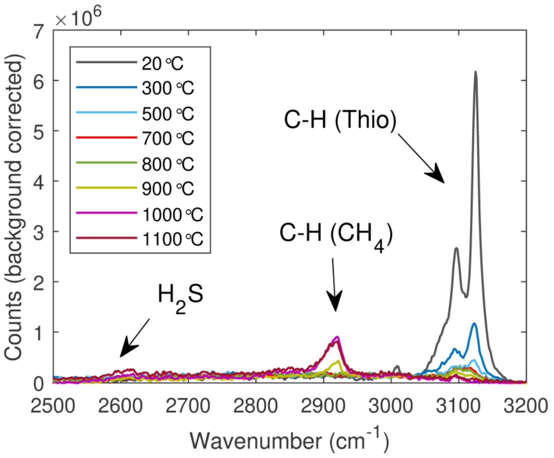

FIG. 9. Raman spectra as a function of temperature for inlet molar fraction $X_{thio} = 0.03$ for the high wavenumber range.

Figure 9 shows the details of the spectra in a higher wavenumber region. The C—H thiophene modes located at 3098 and 3126 cm^{-1} exhibit similar behavior as the C═C modes. The intensity of the mode at 3098 cm^{-1} does not fully decrease to the background level as its location is overlapped with the appearance of a H_2 mode, which instead rises with temperature. A C-H methane mode (ν_1), observed at 2920 cm^{-1}, appears from 900 °C and reaches a maximum observed value at 1000 °C, which does not increase beyond 1100 °C. The behavior is a net result of the increase in methane yield with temperature, offset by the decreasing overall number density. Another weak mode is observed centered at 2600 cm^{-1}, possibly corresponding to the symmetric ν_1 stretching vibrations of H—S bond of hydrogen sulfide.[39] The mode first appears at 900 °C and reaches its highest magnitude at 1100 °C.

Figure 10 shows the magnitude of CH_4 ($\nu1$) and H_2S ($\nu1$) Raman modes as a function of inlet thiophene molar concentration at 1100 °C. The signal magnitudes of both species are proportional to the local molar concentration and the probability of transition, as denoted in Eq. (2). For a fixed temperature, however, the signals (and thus the product molar concentration) can clearly be observed to increase approximately linearly with the inlet thiophene molar fraction.

The presence of H_2S and CH_4 is in agreement with the thermal decomposition thiophene predicted by the Cantera simulations. Furthermore, the presence of methane is in agreement with the products observed by Hoecker *et al.*[11] However, no other major peaks were detected in the 2000–2100 cm^{-1} region with the presence of thiophene in the reactor, indicating that no acetylene or any other triple bond (C≡C) containing compounds were formed, contrary to their original observations. The observed breakdown temperature range of thiophene in a hydrogen environment (800–900 °C) is in agreement with the breakdown temperature observed in pure thiophene vapor atmosphere[17] and hydrogen environment.[11]

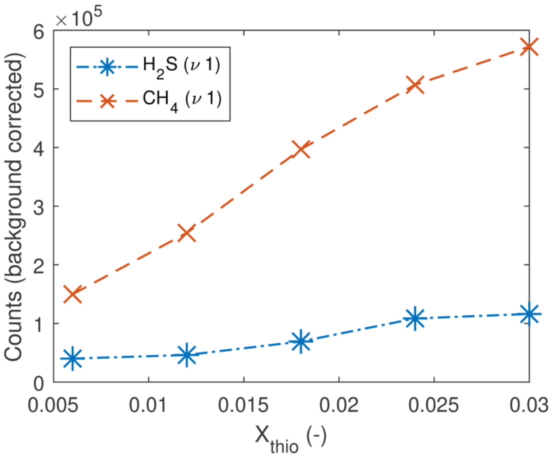

FIG. 10. Magnitudes of CH_4 ($v1$) and H_2S ($v1$) Raman modes as a function of inlet thiophene molar fraction at 1100 °C.

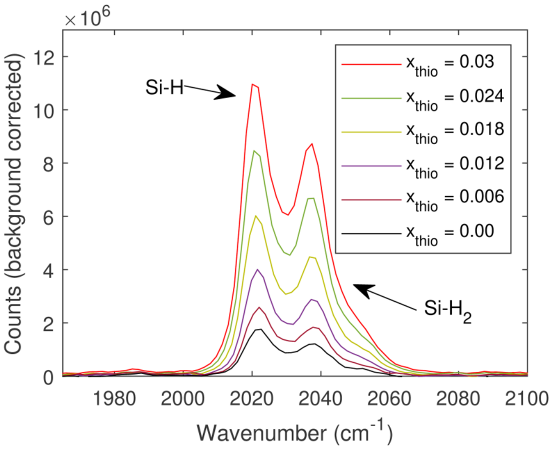

FIG. 12. Si—H modes as a function of X_{thio} at 1100 °C furnace set-temperature.

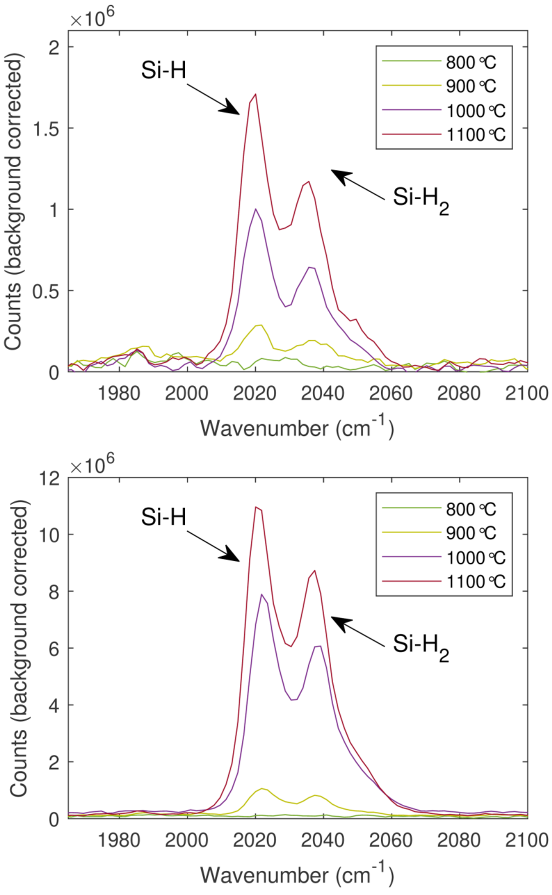

FIG. 11. Raman modes of Si—H and Si—H_2 modes as function of furnace set-temperature at X_{thio} = 0.00 (top) and 0.03 (bottom).

D. Reactor tube dependent Raman modes

In this final section, we investigate the presence of Raman modes associated with the reactor tube itself. Figure 7 shows the presence of identifiable Si—H and Si—H_2 bonds (herewith referred to as Si—H bonds), located at 2018 and 2038 cm^{-1} respectively, at temperatures around 1100 °C. Figure 11(a) shows the variation of intensities of these modes as a function of temperature for inlet molar fractions of (a) $X_{thio} = 0.00$ (pure H_2 environment) and (b) $X_{thio} = 0.03$. In both cases, the Si—H mode starts to appear at 900 °C, however, as seen in Fig. 11(b) the presence of thiophene appears to encourage higher Si—H production, as evidenced by higher mode amplitude. Figure 12 shows the change of Si—H mode magnitudes as a function of inlet X_{thio} at 1100 °C furnace set-point temperature. It can be observed that an increase in thiophene inlet molar fraction leads to a near-linear increase in the magnitude of the Si—H modes, indicating an increased severity of a possible etching effect.

V. CONCLUSIONS

Raman spectroscopy measurements of thiophene decomposition at low inlet molar fractions as a function of temperature in the range of 20–1100 °C have been shown in an environment akin to FC-CVD CNT production. The system tracked thiophene Raman mode magnitudes through its decomposition. Methane and H_2S have been identified as two major products of thiophene decomposition, which are first observed at 900 °C, with the mode amplitudes increasing as a function of temperature. The presence of thiophene decomposition products resulted in accelerated production of Si—H modes when compared to a pure hydrogen environment, suggesting that the latter may have appeared from etching by H_2S.

The experiment has demonstrated that it is in principle possible to observe the products of decomposition and potentially synthesis of CNTs in a furnace reactor using Raman spectroscopy.

However, the relatively low signal and the need for optical access under conditions where particles are formed significantly hamper the use of the technique. It is possible that sampling techniques followed by species separation such as GC-MS may offer additional information.

SUPPLEMENTARY MATERIAL

See the supplementary material for explication of gas dynamics within the cross reactor.

ACKNOWLEDGMENTS

Lee Weller and Maxim Kuvshinov are both funded by EPSRC UK under Award No. EP/M015211/1 within the ANAM Initiative. We thank Fiona Smail, Brian Graves, and Liron Issman (University of Cambridge, Engineering Department) for reading and commenting on the manuscript.

AUTHOR DECLARATIONS

Conflict of Interest

The authors have no conflicts to disclose.

Author Contributions

M. Kuvshinov: Conceptualization (equal); Data curation (lead); Formal analysis (equal); Investigation (equal); Methodology (equal); Writing – original draft (lead); Writing – review & editing (equal). **L. Weller:** Conceptualization (equal); Formal analysis (equal); Investigation (equal); Methodology (equal); Supervision (equal); Writing – original draft (supporting); Writing – review & editing (equal). **S. Hochgreb:** Conceptualization (equal); Funding acquisition (lead); Methodology (equal); Project administration (lead); Supervision (lead); Writing – review & editing (lead).

DATA AVAILABILITY

The data that support the findings of this study are available from the corresponding author upon reasonable request.

REFERENCES

[1] M. F. De Volder, S. H. Tawfick, R. H. Baughman, and A. J. Hart, "Carbon nanotubes: Present and future commercial applications," Science **339**, 535–539 (2013).

[2] E. Pop, D. Mann, Q. Wang, K. Goodson, and H. Dai, "Thermal conductance of an individual single-wall carbon nanotube above room temperature," Nano Lett. **6**, 96–100 (2006).

[3] E. T. Thostenson, Z. Ren, and T.-W. Chou, "Advances in the science and technology of carbon nanotubes and their composites: A review," Compos. Sci. Technol. **61**, 1899–1912 (2001).

[4] A. R. Köhler, C. Som, A. Helland, and F. Gottschalk, "Studying the potential release of carbon nanotubes throughout the application life cycle," J. Cleaner Prod. **16**, 927–937 (2008).

[5] J. Suhr, N. Koratkar, P. Keblinski, and P. Ajayan, "Viscoelasticity in carbon nanotube composites," Nat. Mater. **4**, 134–137 (2005).

[6] A. Thess, R. Lee, P. Nikolaev, H. Dai, P. Petit, J. Robert, C. Xu, Y. H. Lee, S. G. Kim, A. G. Rinzler, D. T. Colbert, G. E. Scuseria, D. Tománek, J. E. Fischer, and R. E. Smalley, "Crystalline ropes of metallic carbon nanotubes," Science **273**, 483–487 (1996).

[7] S. Zhang, L. Kang, X. Wang, L. Tong, L. Yang, Z. Wang, K. Qi, S. Deng, Q. Li, X. Bai, F. Ding, and J. Zhang, "Arrays of horizontal carbon nanotubes of controlled chirality grown using designed catalysts," Nature **543**, 234–238 (2017).

[8] L. Weller, F. R. Smail, J. A. Elliott, A. H. Windle, A. M. Boies, and S. Hochgreb, "Mapping the parameter space for direct-spun carbon nanotube aerogels," Carbon **146**, 789–812 (2019).

[9] M. Endo, T. Hayashi, and Y.-A. Kim, "Large-scale production of carbon nanotubes and their applications," Pure Appl. Chem. **78**, 1703–1713 (2006).

[10] Y.-L. Li, I. A. Kinloch, and A. H. Windle, "Direct spinning of carbon nanotube fibers from chemical vapor deposition synthesis," Science **304**, 276–278 (2004).

[11] C. Hoecker, F. Smail, M. Bajada, M. Pick, and A. Boies, "Catalyst nanoparticle growth dynamics and their influence on product morphology in a CVD process for continuous carbon nanotube synthesis," Carbon **96**, 116–124 (2016).

[12] C. Hoecker, F. Smail, M. Pick, and A. Boies, "The influence of carbon source and catalyst nanoparticles on CVD synthesis of CNT aerogel," Chem. Eng. J. **314**, 388–395 (2017).

[13] T. S. Gspann, F. R. Smail, and A. H. Windle, "Spinning of carbon nanotube fibres using the floating catalyst high temperature route: Purity issues and the critical role of sulphur," Faraday Discuss. **173**, 47–65 (2014).

[14] S.-H. Lee, J. Park, H.-R. Kim, T. Lee, J. Lee, Y.-O. Im, C.-H. Lee, H. Cho, H. Lee, C.-H. Jun, Y.-C. Ahn, I.-B. Lee, and K.-H. Lee, "Synthesis of carbon nanotube fibers using the direct spinning process based on design of experiment (DOE)," Carbon **100**, 647–655 (2016).

[15] V. Reguero, B. Alemán, B. Mas, and J. J. Vilatela, "Controlling carbon nanotube type in macroscopic fibers synthesized by the direct spinning process," Chem. Mater. **26**, 3550–3557 (2014).

[16] A. R. Bogdanova, D. V. Krasnikov, and A. G. Nasibulin, "The role of sulfur in the CVD carbon nanotube synthesis," Carbon **210**, 118051 (2023).

[17] C. D. Hurd, R. V. Levetan, and A. R. Macon, "Pyrolytic formation of arenes. II. Benzene and other arenes from thiophene, 2-methylthiophene and 2-(methyl-14C)-thiophene," J. Am. Chem. Soc. **84**, 4515–4519 (1962).

[18] H. Wynberg and A. Bantjes, "Pyrolysis of thiophene," J. Org. Chem. **24**, 1421–1423 (1959).

[19] H. Ur Rahman Memon, A. Williams, and P. T. Williams, "Shock tube pyrolysis of thiophene," Int. J. Energy Res. **27**, 225–239 (2003).

[20] C. F. Cullis and A. C. Norris, "The pyrolysis of organic compounds under conditions of carbon formation," Carbon **10**, 525–537 (1972).

[21] N. R. Hore and D. K. Russell, "The thermal decomposition of 5-membered rings: A laser pyrolysis study," New J. Chem. **28**, 606–613 (2004).

[22] G. Waddington, J. W. Knowlton, D. W. Scott, W. N. Hubbard, J. C. Smith, H. M. Huffman, G. D. Oliver, and S. S. Todd, "Thermodynamic properties of thiophene," J. Am. Chem. Soc. **71**, 797–808 (1949).

[23] D. Conroy, A. Moisala, S. Cardoso, A. Windle, and J. Davidson, "Carbon nanotube reactor: Ferrocene decomposition, iron particle growth, nanotube aggregation and scale-up," Chem. Eng. Sci. **65**, 2965–2977 (2010).

[24] F. Smail, A. Boies, and A. Windle, "Direct spinning of CNT fibres: Past, present and future scale up," Carbon **152**, 218–232 (2019).

[25] S. Iordanova, "Spectroscopic temperature measurements in hydrogen inductively-driven plasmas at low pressures," in *Journal of Physics: Conference Series* (IOP Publishing, 2008), Vol. 113, p. 12005.

[26] B. Xiao, S. Kado, S. Kajita, and D. Yamasaki, "Rovibrational distribution determination of H2 in low temperature plasmas by Fulcher-α band spectroscopy," Plasma Phys. Control. Fusion **46**, 653 (2004).

[27] S. Briefi, D. Rauner, and U. Fantz, "Determination of the rotational population of H2 and D2 including high-N states in low temperature plasmas via the Fulcher-α transition," J. Quant. Spectrosc. Radiat. Transfer **187**, 135–144 (2017).

[28] V. N. Ochkin, Y. S. Savinov, and N. N. Sovolev, "*Electron Excited Molecules in Nonequilibrium Plasma*, Proceedings of the Lebedev Physics Institute Vol. 179 (Nova Publisher, New York, 1989), p. 2

[29] M. Pealat, J. P. E. Taran, J. Taillet, M. Bacal, and A. M. Bruneteau, "Measurement of vibrational populations in low-pressure hydrogen plasma by coherent anti-Stokes Raman scattering," J. Appl. Phys. **52**, 2687–2691 (1981).

[30]S. A. Astashkevich, M. Käning, E. Käning, N. V. Kokina, B. P. Lavrov, A. Ohl, and J. Röpcke, "Radiative characteristics of 3p Σ, Π; 3d Π-, Δ- states of H2 and determination of gas temperature of low pressure hydrogen containing plasmas," J. Quant. Spectrosc. Radiat. Transfer **56**, 725–751 (1996).

[31]Z. Gavare, G. Revalde, and A. Skudra, "Plasma temperature determination of hydrogen containing high-frequency electrodeless lamps by intensity distribution measurements of hydrogen molecular band," Int. J. Spectrosc. **2010**, 1–8 (2010).

[32]G. H. Dieke, *The Hydrogen Molecule Wavelength Tables of Gerhard Heinrich Dieke* (Wiley-Interscience, New York, 1972).

[33]S. A. Alexander and R. L. Coldwell, "Spectroscopic constants of H_2 using Monte Carlo methods," Int. J. Quantum Chem. **100**, 851–857 (2004).

[34]I. Dabrowski, "The Lyman and Werner bands of H_2," Can. J. Phys. **62**, 1639–1664 (1984).

[35]D. G. Goodwin, H. K. Moffat, I. Schoegl, R. L. Speth, and B. W. Weber, see https://www.cantera.org for "Cantera: An Object-Oriented Software Toolkit for Chemical Kinetics, Thermodynamics, and Transport Processes" (2022).

[36]C. Zhang, B. Tian, C. T. Chong, B. Ding, L. Fan, X. Chang, and S. Hochgreb, "Synthesis of single-walled carbon nanotubes in rich hydrogen/air flames," Mater. Chem. Phys. **254**, 123479 (2020).

[37]B. Somogyi, E. Bruyer, and A. Gali, "Photoluminescence, infrared, and Raman spectra of co-doped Si nanoparticles from first principles," J. Chem. Phys. **149**, 154702 (2018).

[38]S. Lee, J. Ahn, L. Mathew, R. Rao, Z. Zhang, J. H. Kim, S. K. Banerjee, and E. T. Yu, "Highly improved passivation of c-Si surfaces using a gradient i a-Si:H layer," J. Appl. Phys. **123**, 163101 (2018).

[39]M. Hippler, "Cavity-enhanced Raman spectroscopy of natural gas with optical feedback cw-diode lasers," Anal. Chem. **87**, 7803–7809 (2015).